Journal of Rock Mechanics and Geotechnical Engineering 14 (2022) 1266–1279

Contents lists available at ScienceDirect

Journal of Rock Mechanics and Geotechnical Engineering

journal homepage: www.jrmge.cn

Full Length Article

Responses of calcareous sand foundations to variations of groundwater table and applied loads

Dingfeng Cao [a,b,*], Sanjay Kumar Shukla [c], Linqing Yang [a,b,d], Chengchao Guo [a,b,**], Jinghong Wu [e], Fuming Wang [a,b]

[a] School of Civil Engineering, Sun Yat-sen University, Guangzhou, 510275, China
[b] Southern Marine Science and Engineering Guangdong Laboratory (Zhuhai), Zhuhai, 519082, China
[c] Discipline of Civil and Environmental Engineering, School of Engineering, Edith Cowan University, Perth, 6027, Australia
[d] School of Architectural Engineering, Guangzhou Institute of Science and Technology, Guangzhou, 510540, China
[e] School of Civil Engineering, Suzhou University of Science and Technology, Suzhou, 215011, China

ARTICLE INFO

Article history:
Received 2 July 2021
Received in revised form
1 August 2021
Accepted 20 August 2021
Available online 20 September 2021

Keywords:
Distributed fiber optic sensing (DFOS)
Calcareous sand
Optical fiber
Optical frequency domain reflectometer (OFDR)
Soil foundation settlement

ABSTRACT

The long-term settlement of calcareous sand foundations caused by daily periodic fluctuations has become a significant geological hazard, but effective monitoring tools to capture the deformation profiles are still rarely reported. In this study, a laboratory model test and an in situ monitoring test were conducted. An optical frequency domain reflectometer (OFDR) with high spatial resolution (1 mm) and high accuracy ($\pm 10^{-6}$) was used to record the soil strain responses to groundwater table and varied loads. The results indicated that the fiber-optic measurements can accurately locate the swelling and compressive zones. During the loading process, the interlock between calcareous sand particles was detected, which increased the internal friction angle of soil. The foundation deformation above the sliding surface was dominated by compression, and the soil was continuously compressed beneath the sliding surface. After 26–48 h, calcareous sand swelling occurred gradually above the water table, which was primarily dependent on capillary water. The swelling of the soil beneath the groundwater table was completed rapidly within less than 2 h. When the groundwater table and load remain constant, the compression creep behavior can be described by the Yasong-Wang model with $R^2 = 0.993$. The daily periodically varying in situ deformation of calcareous sand primarily occurs between the highest and lowest groundwater tables, i.e. 4.2–6.2 m deep. The tuff interlayers with poor water absorption capacity do not swell or compress, but they produce compressive strain under the influence of deformed calcareous sand layers.

1. Introduction

In the South China Sea, calcareous sand has been widely used as foundation backfill material for roads, docks, airport runways, buildings, and other infrastructure (Wang et al., 2019; He et al., 2020). However, as the artificially dredged calcareous sands have significantly different deformation properties from quartz sand on the mainland (Shahnazari and Rezvani, 2013), it is difficult to obtain the actual geotechnical parameters of offshore calcareous sand foundations and conduct appropriate designs according to the standards conventionally used on the mainland. Calcareous sands have the features of high crushability, low single-particle strength, large voids, and complex microstructures, resulting in special deformation characteristics and even severe disasters (Wu et al., 2021a). The most famous example is the settlement of the Kansai Airport. In December 2012, the average settlements for Airport Islands I and II were reported to exceed 12.9 m and 14.2 m, respectively, and the settlement will exceed 23 m in 2100 (Mesri and Funk, 2015). Many researchers have been surprised by the significant unending settlement when the applied load is smaller than the pre-consolidation pressure, which leads them to

* Corresponding author. School of Civil Engineering, Sun Yat-sen University, Guangzhou, 510275, China.
** Corresponding author. School of Civil Engineering, Sun Yat-sen University, Guangzhou, 510275, China.
E-mail addresses: caodf3@mail.sysu.edu.cn (D. Cao), guochch25@mail.sysu.edu.cn (C. Guo).
Peer review under responsibility of Institute of Rock and Soil Mechanics, Chinese Academy of Sciences.

https://doi.org/10.1016/j.jrmge.2021.08.003

reconsider the field effectiveness of the models established based on laboratory tests and seek effective in situ monitoring methods.

Current methods to determine land subsidence can be basically divided into three categories: remote sensing, geodetic surveying, and numerical simulation. The most common remote-sensing technology is interferometric synthetic aperture radar (InSAR), which has been successfully used to monitor large-scale regional subsidence (Catalao et al., 2020; Liu et al., 2020). However, InSAR has limitations: spatial error, temporal decorrelation, and inaccurate interpretation (Liu et al., 2020). The traditional geodetic surveying method is the most reliable with high accuracy, but it is difficult to apply in frequent measurements on offshore islands due to high time cost. Although the latest developed 3D scanning has reduced labour intensity and can increase efficiency on the mainland, it is still difficult to be applied on offshore islands owing to high transportation cost (Gu et al., 2020). In addition, only ground surface settlement can be obtained using remote-sensing geodetic surveying methods, and the deformation of sub-surficial soil layers cannot be acquired.

To overcome the limitations of above-mentioned monitoring methods, particle image velocimetry (PIV) and distributed fiber optic sensing (DFOS) are frequently used to record soil particle transportation and deformation (e.g. Zhu et al., 2014; 2016; Zhang et al., 2018a; Wu et al., 2020; Cao et al., 2021; Wang et al., 2021; Zhang et al., 2021). PIV enables the displacement of each superficial particle to be accurately captured, but it is unable to acquire interior deformation that has fewer boundary effects than superficial particles. It has been reported that the soil strain profiles, compression and rebound cycles, and elastic and plastic zones in model chambers can be accurately obtained using DFOS (Liu et al., 2019). Wu et al. (2017) suggested that the deformation of a sand layer is synchronous with water content, and creep becomes elastic deformation after a soil layer experiences many draining-recharging cycles.

DFOS has also been applied to monitor in situ ground settlement. Wu et al. (2021b) observed that the compression–rebound zone is closely related to the groundwater table. Liu et al. (2020) calculated the subsidence rate in Tianjin, China, and reported that the subsidence in this area is triggered by fluctuation in the groundwater table and loading. Zhang et al. (2018b) proposed that the DFOS had two significant advantages: predicting the realistic location of a layer undergoing compaction or rebound and recording the strain response of soil at various locations. Based on the in situ strain profiles measured using DFOS and laboratory microstructure analysis, Gu et al. (2018) emphasized that ground settlement occurs seasonally: it is compressed in spring and summer and rebound in autumn and winter, and both elastic and plastic zones can be captured. Moreover, Gu et al. (2018) indicated that the main deformation occurred in soils with large fractal dimensions and a high proportion of large pores.

Although DFOS has been proven to be effective in monitoring soil strain profiles in laboratory chambers and in fields, it is still not clear that it can be used for settlement monitoring in the calcareous sand foundations of offshore islands because of the different geological and stress conditions. Large-scale land subsidence on the mainland is considered to be caused by the excessive withdrawal of groundwater and hydrocarbon fluids (Gu et al., 2018). The groundwater table on the mainland subsidence area is controlled by the pumping volume and rainfall replenishment; thus, it is seasonal variation. However, the groundwater table in the calcareous sand foundations of offshore islands is determined by sea level, tides, and waves caused by hurricanes. Hence, the groundwater table in the calcareous sand foundation fluctuates more frequently than that on the mainland, and soil deformation caused by the groundwater table is also likely to occur. Generally, the effect of the upper load is not considered when investigating the causes of regional land subsidence, but the deformation of the calcareous sand foundation is closely related to the upper load. Furthermore, calcareous sand exhibits a larger strain upon failure, and higher compressibility. It is more crushable and angular than terrigenous quartz sand (Kuang et al., 2020). Therefore, the feasibility using DFOS to capture and record the deformation of the calcareous sand foundation requires verification.

The previous DFOS used in subsidence monitoring is the Brillouin optical time domain reflectometer (BOTDR) that is suitable for long-distance tests. The BOTDR is difficult to be applied in laboratory chambers or foundations with requirements of high spatial resolution. Compared with BOFDR, the optical frequency domain reflectometer (OFDR) has advantages of high spatial resolution ($\pm$1 mm) and high accuracy ($\pm 10^{-6}$). OFDR has been proved powerful in monitoring strain profiles of structures. Wang and Liu (2021) successfully captured the internal stress of a landslide. Boujia et al. (2020) acquired strain profiles of a rod under the action of scouring. Kwon et al. (2018) obtained the strain of a ground anchor bearing plate and evaluated the tensile force of the anchor. Nevertheless, the feasibility of monitoring sand deformation must be further verified, because the connection between granular sand and the optical fiber is completely different from that of structure.

This study aimed to capture the deformation evolution of reclaimed calcareous sand foundations in response to groundwater table and varied loads and investigate associated soil strain profiles. An attempt has been made in this context to evaluate common creep models and verify the feasibility of in-situ measurements using OFDR with monitoring the soil strain profiles. A laboratory model test and a field test were conducted. The results may help engineers for better designing foundation systems by avoiding unexpected future settlements.

2. Materials and methods

2.1. Laboratory model test

The laboratory test configuration is depicted in Fig. 1. The test was performed in a cuboid chamber, which was further divided into three subspaces: water supply, drainage chambers, and a soil package chamber. Steel pillars and beams were welded together to form the internal space with a size of 2.3 m $\times$ 1.2 m $\times$ 1.2 m (length $\times$ width $\times$ height). Transparent glass plates were fixed on the beams as the chamber wall. Breast boards with small holes were installed between the soil package and soil water drainage (or supply) chambers. A gauze was pasted on the surface of the boards to enable the water to flow freely but prevent the passage of soil particles. Lubricating oil was applied to the inside of the soil package chamber to reduce the friction between the soil and chamber walls. Fig. 1b shows the strain sensing cable (SSC) installed with coupling wafers, and details of the production process are available in Wu et al. (2017). The total length of the soil package chamber was 1.7 m. An SSC and a series of frequency domain reflectometry (FDR) were installed at positions x = 0.1 m, 0.4 m, 0.7 m, 1.0 m, 1.3 m, and 1.6 m. At each position x, five FDRs were installed at depths of 0.15 m, 0.35 m, 0.55 m, 0.8 m, and 1.05 m.

Two soil samples were placed in the chambers, one of which was coral calcareous sand (Soil A) sampled near the Xisha Islands in the South China Sea, and the other was a mixture of calcareous sand and kaolin (Soil B), with a dry mass ratio of 9:1. During the construction of the calcareous sand foundation, the dredged distance of sand was farther than that of clay; hence, the settlement of a foundation is a combined deformation of different layers. However, simulating dredging process in laboratory tests is difficult; Song et al. (2017) suggested the use of kaolin to replace in situ clay.

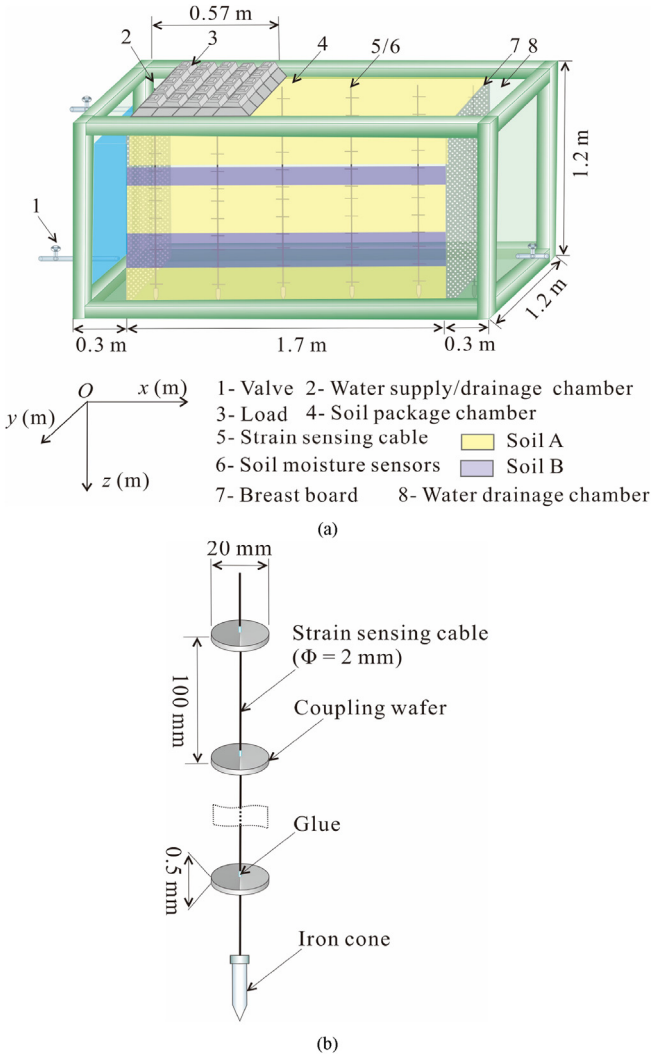

Fig. 1. Schematic of the experimental setup: (a) Soil chamber and (b) Strain-sensing cable.

The basic physical parameters of Soils A and B are listed in Table 1. Fig. 2 shows the particle size distribution of Soils A and B. Soil A was filled at the depth of 0–0.3 m, 0.4–0.7 m, and 0.9–1.2 m, and Soil B of 0.3–0.4 m and 0.7–0.9 m. The soils were filled one layer at a time. The initial volumetric moisture content of the two soils was 0.11 ± 0.03 m^3/m^3, and the dry densities of Soils A and B were 1510 ± 15 kg/m^3 and 1550 ± 15 kg/m^3, respectively. Because the deformation caused by the particles sliding during the first watering–dewatering cycle was large, the soil should be soaked and drained before the creep properties were investigated.

The test procedure was divided into loading, watering, and dewatering. The total durations for each stage were 96 h, 48 h, and 792 h, respectively. The three-level loading was achieved by placing weights with the mass of 20 kg, 10 kg, and 5 kg. The corresponding

Table 1
Basic physical parameters.

Index	Soil A	Soil B
Liquid limit (%)	29.5 ± 0.6	28.8 ± 0.7
Plastic limit (%)	22.7 ± 0.5	21.6 ± 0.8
Hydraulic conductivity (m/s)	0.0481 ± 0.007	0.0258 ± 0.003
Void ratio	0.62 ± 0.01	0.60 ± 0.01
Dry density (kg/m^3)	1510 ± 15	1550 ± 15

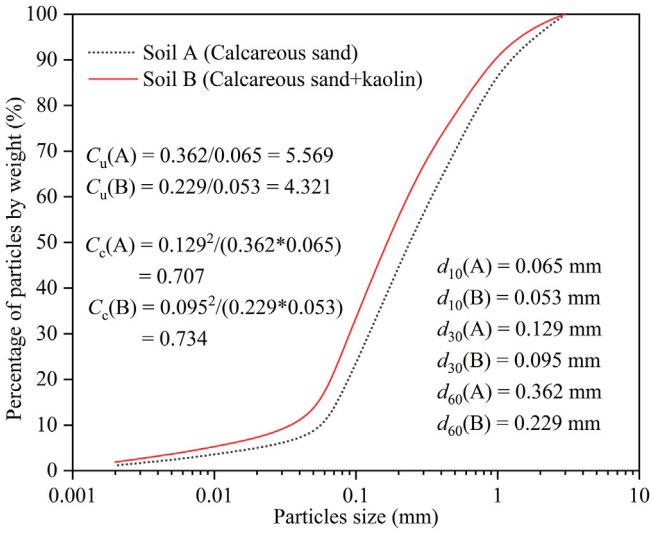

Fig. 2. Soil particle distribution.

pressures on the soil surface were 29.24 kPa, 43.86 kPa, and 51.17 kPa, respectively. During the watering stage, the water table was maintained at a depth of 0.6 m. During the dewatering stage, all valves were open to drainage. The strain in each stage was recorded using an OFDR interrogator produced by the Etsc (Hong Kong) Technologies Limited. When using an OFDR, the initial Rayleigh scattering spectrum should be measured and stored, and the scattering spectra with strain or temperature perturbations can be measured (Henault et al., 2012). The relationship between the Rayleigh spectral shift and changes in strain and temperature is expressed as follows:

$$\Delta v = k_\varepsilon \varepsilon + k_T \Delta T \tag{1}$$

where Δv is the Rayleigh spectral shift (Hz), ε is the fiber strain (dimensionless), and k_ε and k_T are the calibration constants. The vertical displacement can be calculated from the strain profiles (Pelecanos et al., 2018):

$$u(z) = u(z = z_0) + \int_0^z \varepsilon(z)\mathrm{d}z \tag{2}$$

where $u(z)$ is the vertical displacement (mm) and represents the vertical axis. The average strain $\bar{\varepsilon}$ for each soil layer is defined as

$$\bar{\varepsilon} = \frac{u(z)}{d} \tag{3}$$

where d is the thickness of the soil layer (mm).

2.2. Field test

A field test was conducted in Danzhou, Hainan Province (19°52′35″N, 109°15′33″E), China, to verify the feasibility of monitoring the deformations of calcareous foundations due to groundwater table fluctuation. The site is located on a bay that is piled up with large amounts of coral sand and gravel. The groundwater table is controlled by the sea level, which is determined by the tide. There are six layers with a total depth of 12 m. The layers from the surface to the bottom are plain fill, calcareous sand, basalt, clay, a mixture of clay and calcareous, and tuff (Fig. 3), respectively. The surficial plain fill (0–0.4 m) was formed artificially. The calcareous sand layer (0.4–

0.9 m) was deposited after being mobilised by waves. The basalt layer (0.9–3.3 m) was severely weathered and dominated by stomatal structures. The main mineral components are plagioclase, pyroxene, and olivine. The clay depth ranges from 3.3 m to 9 m and contains weathered residual soil of tuff. The strengths of the calcareous sand and clay mixture depend on water content. In addition, tuff interlayers can be observed at depth of 5.5–9 m. The bottom layer is layered tuff formed by volcanic ash, volcanic clasts, and sand grains through sedimentation and condensation.

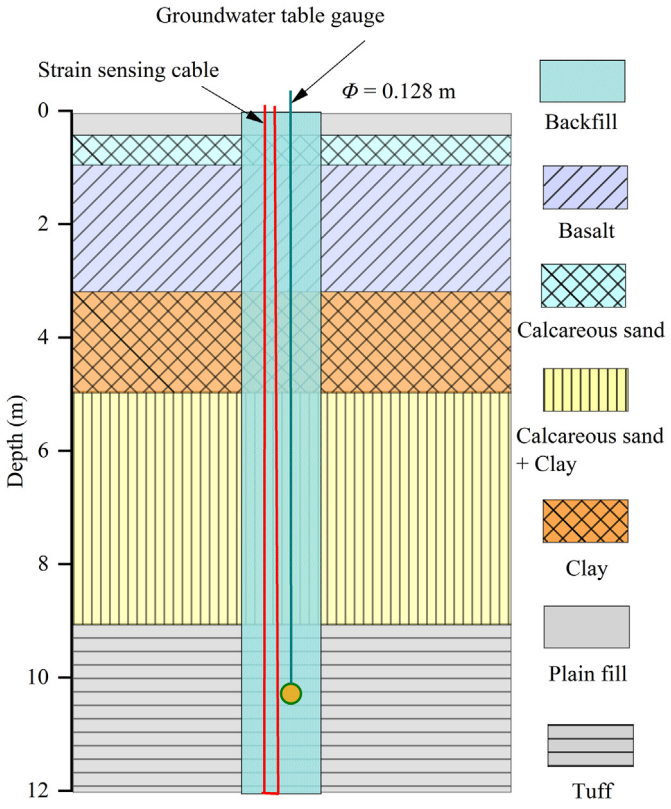

Fig. 3. The stratigraphy of the borehole.

The SSC pre-tensioned at the strain of 0.01 was installed through a borehole to monitor the layer deformation. The borehole had a diameter of 128 mm and a depth of 12 m. A groundwater table gauge was installed at a depth of 10.5 m with an accuracy of ±0.1 m. The surrounding space of the SSC was backfilled with Soil A as used in the laboratory test. The borehole was backfilled on January 24, 2021, and then left to equalize for approximately three months. The field measurement began at 0:00 on April 19, 2021, and completed at 0:00 on April 21, 2021. The sampling interval was 300 s.

3. Results and discussions

3.1. Responses of soil to loads in the laboratory test

To facilitate the description of soil deformation in different parts, the soil position in the model chamber was divided into 30 zones, numbered from A1–A18 and B1–B12 (Fig. 4). The soil moisture variation was less than 0.01 m^3/m^3 during the entire three-level loading process; thus, the influence of moisture change on the settlement could be neglected. Fig. 4 shows that all soil layers below the loading area (x = 0.1 m and 0.4 m) were compressed after the first-level loading. The compression was primarily completed in the first 2 h and changed slightly during the period of 2–22 h. The occurrence of tensile strain in A15 and A16 indicated that the soil in these areas moved horizontally. In addition, because zones B8 and A14 were compressed, it was inferred that zones A15 and A16 moved horizontally to the side of the drainage chamber. Note that the tensile strain of SSC did not represent the stretched surrounding soil. In contrast, this suggested that the soil expanded after compression. The deformation direction of the soil in different zones was drawn according to the soil strain profiles measured

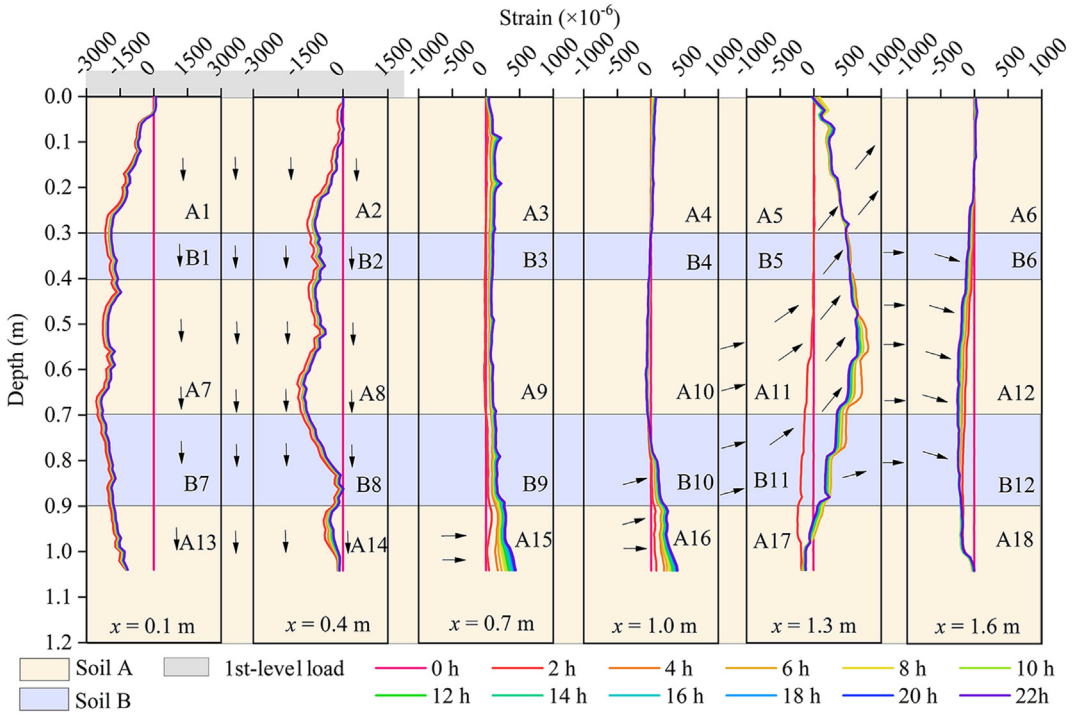

Fig. 4. Soil strain profiles under the first-level load (29.24 kPa).

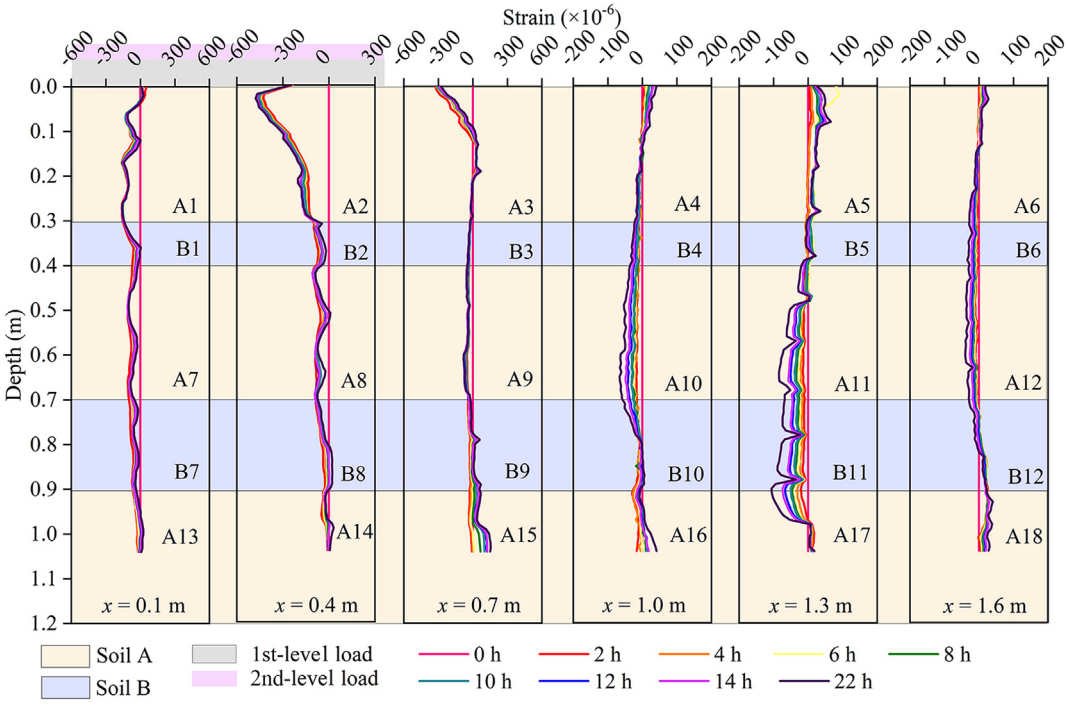

Fig. 5. Soil strain profiles when the load ranged from the first-level to the second-level load (from 29.24 kPa to 43.86 kPa).

using the SSC, as shown by the black arrows in Fig. 4, which agreed closely with the soil movement model beneath shallow continuous footings (Terzaghi et al., 1996). This agreement also indicated that the cohesion of calcareous sand near the Xisha Islands in the South China Sea is negligible.

When the applied load ranged from 29.19 kPa to 43.86 kPa, the compressive strain at positions $x = 0.1$ m and 0.4 m continued to develop (Fig. 5). The soils at positions $x = 0.7$ m, 1 m, 1.3 m, and 1.6 m were compressed. Note that Fig. 5 only shows the soil strain change from the first to the second loading, and the soil at the positions $x = 0.7$ m, 1 m, and 1.3 m was still more swelled compared with the state prior to loading. The decrease in swelling strain with the increase in load can be explained by the interlocking effect proposed by Lv et al. (2017), which will be discussed in the

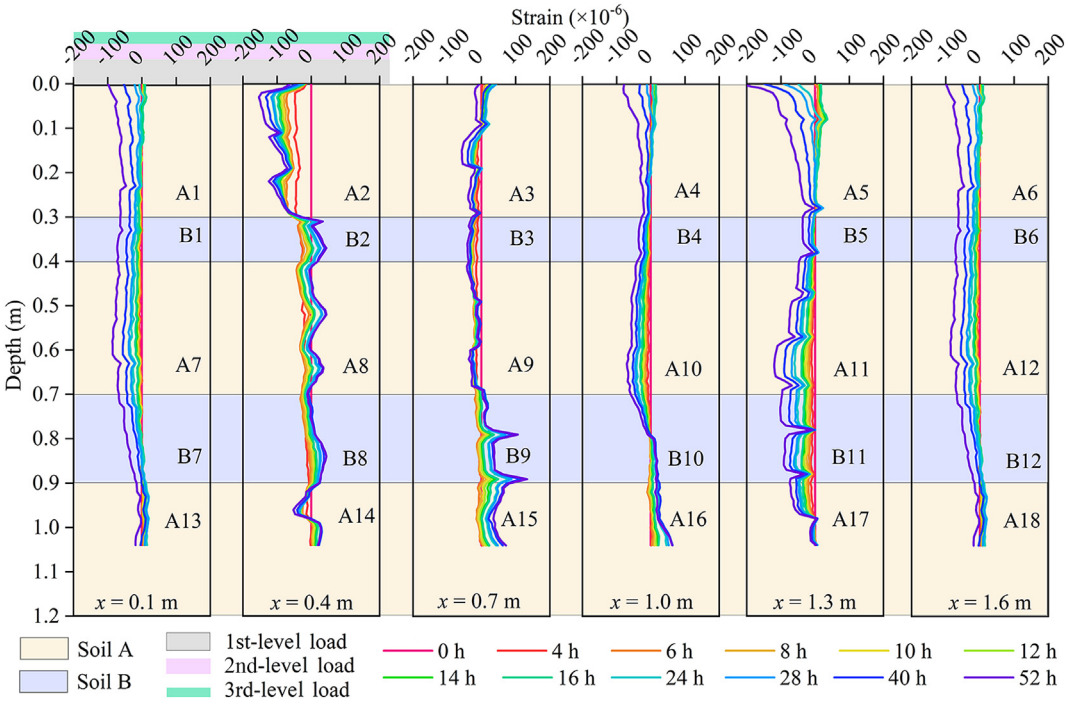

Fig. 6. Soil strain profiles when the load ranged from the second-level to the third-level load (from 48.86 kPa to 51.17 kPa).

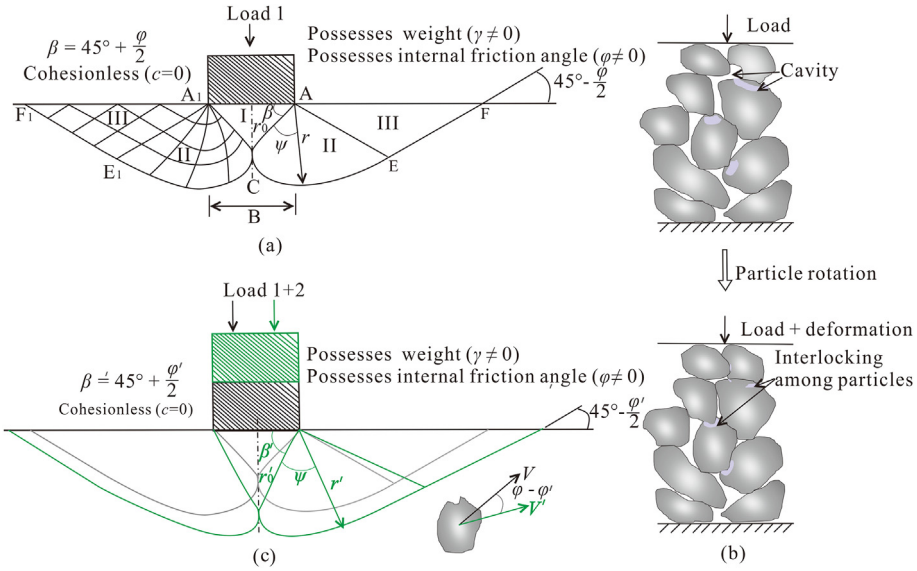

Fig. 7. Foundation deformation beneath continuous footing: (a) Terzaghi's simplified model (Terzaghi et al., 1996), (b) Particle interlocked after loading (Lv et al., 2017), and (c) The influence of particle interlocked on foundation deformation.

following paragraphs. Fig. 6 shows the soil strain development when the load ranged from 43.86 kPa to 51.17 kPa. Similarly, the soils at the positions of x = 0.1 m and 0.4 m were continuously compressed, and new compression occurred at the positions x = 0.7 m, 1 m, and 1.3 m.

The widely used model to describe soil deformation in this test is Terzaghi's model. Terzaghi et al. (1996) proposed that the analytical solution of the local shear failure of sandy soil during the loading process is difficult to obtain, but it can be approximately determined in engineering applications. In the approximate solution, the foundation bearing capacity is assumed to be the sum of three components that can be computed separately, as shown in Fig. 7a. These three components include the friction of a weightless soil without load, the friction of a weightless soil with loading, and the friction of soil with weight but without loading. As shown in Figs. 5 and 6, the direction of soil deformation caused by the second-level load was different from that caused by the first-level load. Similarly, the deformation direction under the third-level load did not follow the path under the second-level load. Based on the observation of a scanning electron microscope (SEM), Lv et al. (2017) observed that calcareous sand particles have noticeable cavities and adjacent interlocked particles owing to the rotation of grains (Fig. 7b). The interlocking can significantly increase the internal friction angle, that is, from ϕ to ϕ'. Thus, the foundation

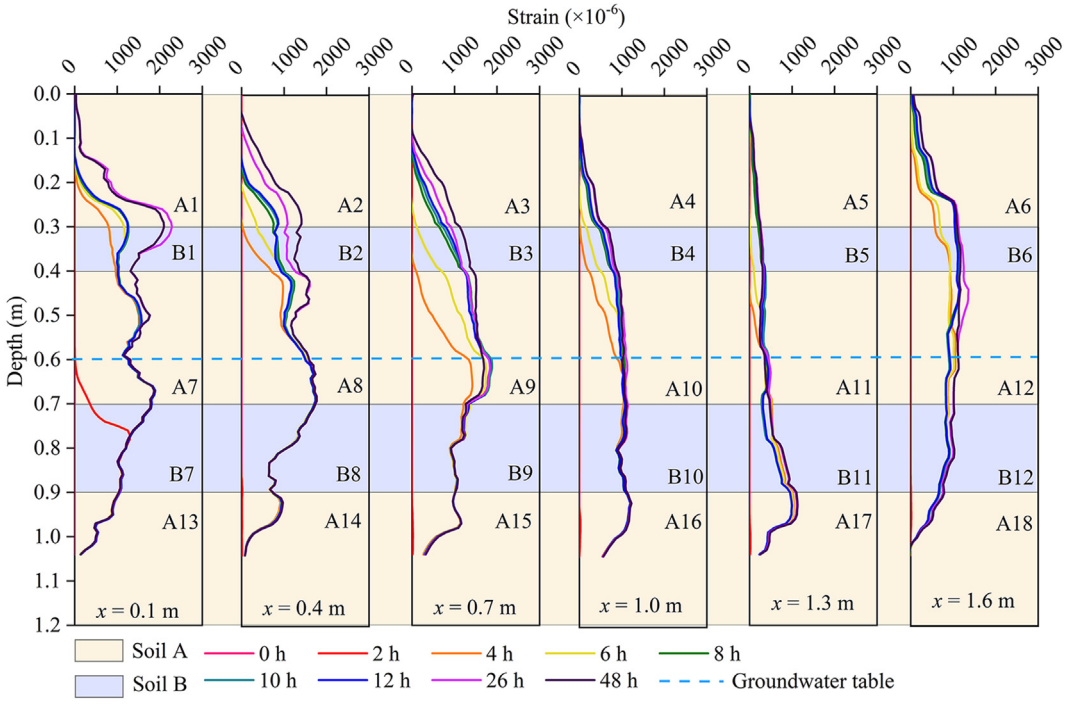

Fig. 8. Soil strain profiles during the watering process.

deformation proposed by Terzaghi et al. (1996) can be modified as shown in Fig. 7c. When ϕ increased to ϕ', both the plastic zone (I) and plastic zones (II and III) were enlarged, and the movement direction of soil particles in zones II and III changed horizontally. This is why compressive strain was observed in zones A10, A11, and A12 in Figs. 5 and 6. According to the numerical solutions obtained by Ahmadi et al. (2021), the increase in ϕ enhances the foundation bearing capacity coefficient, depth of elastic curve wedge, and plastic length, which agrees closely with the observations in Figs. 4–6. The variation in ϕ depends on many factors, for example the static sliding friction coefficient, rolling friction coefficient, restitution coefficient, particle size and shape, water content, and principal stress direction (Al-Hashemi and Al-Amoudi, 2018; Zamanian and Jafarzadeh, 2020). The particle surface of silica sand is more slippery than that of calcareous sand; therefore, the influence of interlocking in the silica sand foundation is not as significant as the results observed in Figs. 4–6.

3.2. Soil swelling after the groundwater table rises in the chamber

The FDR monitoring measurements indicated that the groundwater table reached a depth of 0.6 m in 4 h and then remained

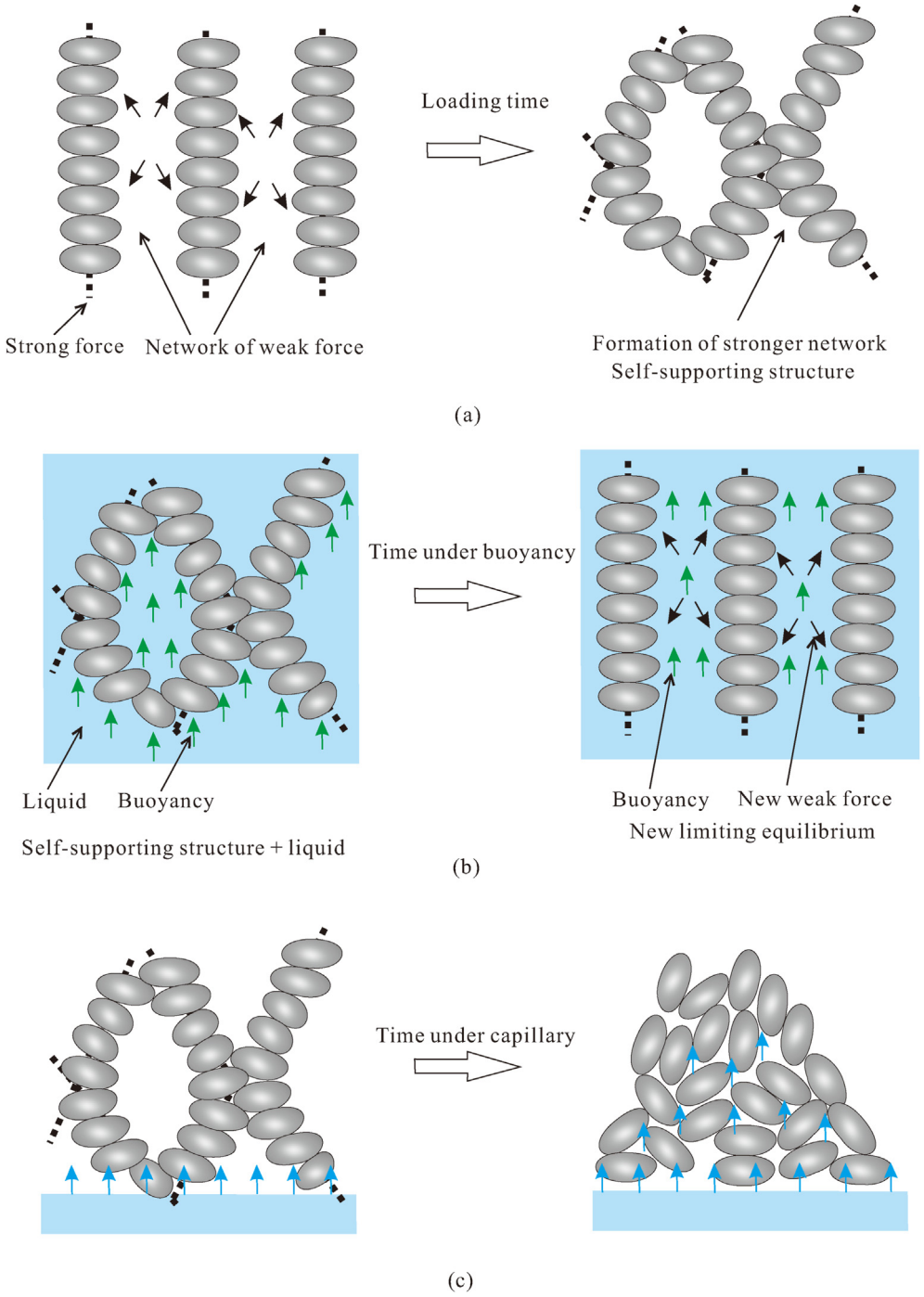

Fig. 9. Mechanism of the transformation between strong and weak forces among calcareous sand particles: (a) Force network change and interlock with time under load (Bowman and Soga, 2003), (b) Force network re-fabrication under buoyancy, and (c) Force network re-fabrication under capillary.

stable. Fig. 8 shows the swelling deformation process measured using the SSC when water was added to a depth of 0.6 m. The swelling rates of soil below and above the groundwater table were significantly different. The groundwater table rose from the depth of 1.2–0.6 m in 2 h, and the expansion of the soil below the groundwater table was completed in this period as well. However, the expansion of the part above the groundwater table occurred in nearly the entire test duration, ranging from 26 h to 48 h. This difference was primarily caused by the different expansion mechanisms, which can be explained by the bimodal characteristics of stress transmission (Bowman and Soga, 2003). The particles were initially aligned perpendicular to the load direction (vertical). As time elapsed, the particles rotated horizontally, and the sandy columns formed a self-supporting structure. The stress of the sandy particles was divided into strong and weak forces under loads. The strong force network on the sand columns bore the primary vertical load, and the weak force network maintained the stability of the structure of the columns (Fig. 9a).

After the self-supporting structure was soaked below the groundwater table, the equilibrium of force changed due to the increase in buoyancy and decrease in frictional contact force. The bending sandy columns recovered to their initial state (Fig. 9b). Above the groundwater table, the friction coefficient decreased sharply owing to the lubrication of capillary water, and the bending sand columns were rotated and collapsed (Fig. 9c). Because the increase in buoyancy was synchronized with the groundwater table, the swelling was completed in 4 h. However, capillary water rose gradually, and its rate was determined by the time, initial water content, and location. The closer to the groundwater table, the earlier the water content changed, which further resulted in the earlier occurrence of the collapse of the soil structure. This phenomenon was verified by the observations of strain in zones B1, B2, B3, A8, A9, and A10 (Fig. 8). Feng et al. (2017) developed a swelling model to describe soil deformation after the effective stress decreased. Effective stress reduction is generally a decrease in the upper load or an increase in the pore water pressure. The swelling creep modelling is expressed as follows:

$$-\frac{1}{\varepsilon^{s}}\ln\left(\frac{t_0^{s}+t^{s}}{t_0^{s}}\right)=\frac{V}{\psi_0^{s}}+\frac{1}{\varepsilon^{sl}}\ln\left(\frac{t_0^{s}+t^{s}}{t_0^{s}}\right) \tag{4}$$

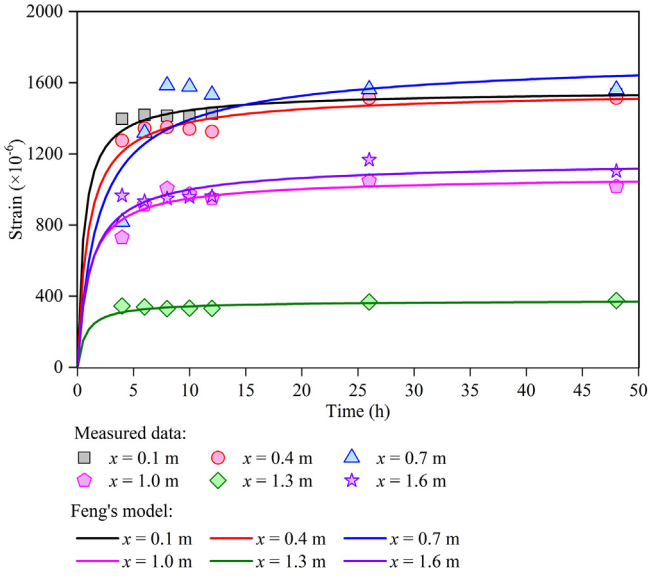

Fig. 10. Comparison of the measured swelling strain of the calcareous sand-fitted curves using Feng's model.

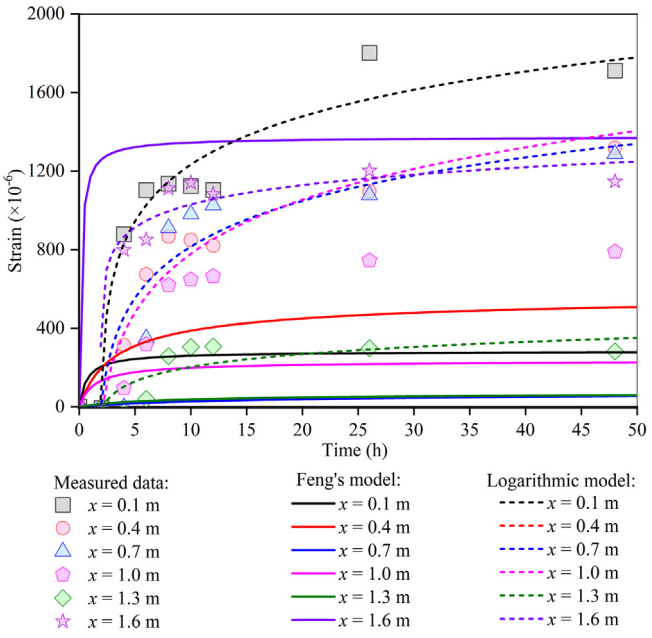

Fig. 11. Comparison of the measured swelling strain of the calcareous sand with kaolin fitted curves using Feng's model.

where V is the specific volume, ε^{sl} is the swelling strain limit, t_0^{s} is the initial swelling time (s), t^{s} is elapsed time (s), and ψ_0^{s} is a swelling creep parameter. The superscript 's' represents the swelling. The measured and estimated swelling strains using Feng's model are shown in Fig. 10.

Because Soil A in the depth range of 0–0.3 m was not completely infiltrated by capillary water, swelling did not occur in the entire depth range. Therefore, the swelling in this range is not discussed. As shown in Fig. 10, the measured values agreed closely with the estimated values of Feng's model, indicating that Feng's model can effectively describe the swelling process of calcareous sand owing to water absorption in the unsaturated zone. Here, the measured values were the average strains calculated using Eqs. (2) and (3), respectively. Fig. 11 shows the measured and estimated swelling strain fitted using Feng's model (solid curves) of Soil B at depth of 0.3–0.4 m. The measured values were significantly larger than the estimated values, indicating that Feng's model was not suitable for describing the swelling process of Soil B in this test. The main reason for the deviation was that the test time was not sufficiently long. ε^{sl} must be determined in Feng's swelling model, but it was difficult to obtain during 48-h test period. When the creep limit is difficult to determine, the use of a logarithmic model to describe the strain over elapsed time has been suggested (Wang et al., 2012). The dotted curves in Fig. 11 represent the estimated values fitted with a logarithmic model using three coefficients. Compared with Feng's model, the estimated values of the logarithmic model were closer to the measured values. The coefficients of determination (R^2) for the fitted curves in Figs. 10 and 11 are listed in Table 2.

Table 2
R^2 of the soil-swelling models obtained in the test.

Soil	Model	R^2 fitting at various distances to the origin of the x-axis						Average R^2
		0.1 m	0.4 m	0.7 m	1 m	1.3 m	1.6 m	
Soil A	Feng's model	0.997	0.992	0.853	0.981	0.99	0.973	0.964
Soil B	Feng's model	0.747	0.106	0.037	0.014	0.108	0.953	0.326
	Logarithmic model	0.923	0.951	0.786	0.804	0.525	0.936	0.821

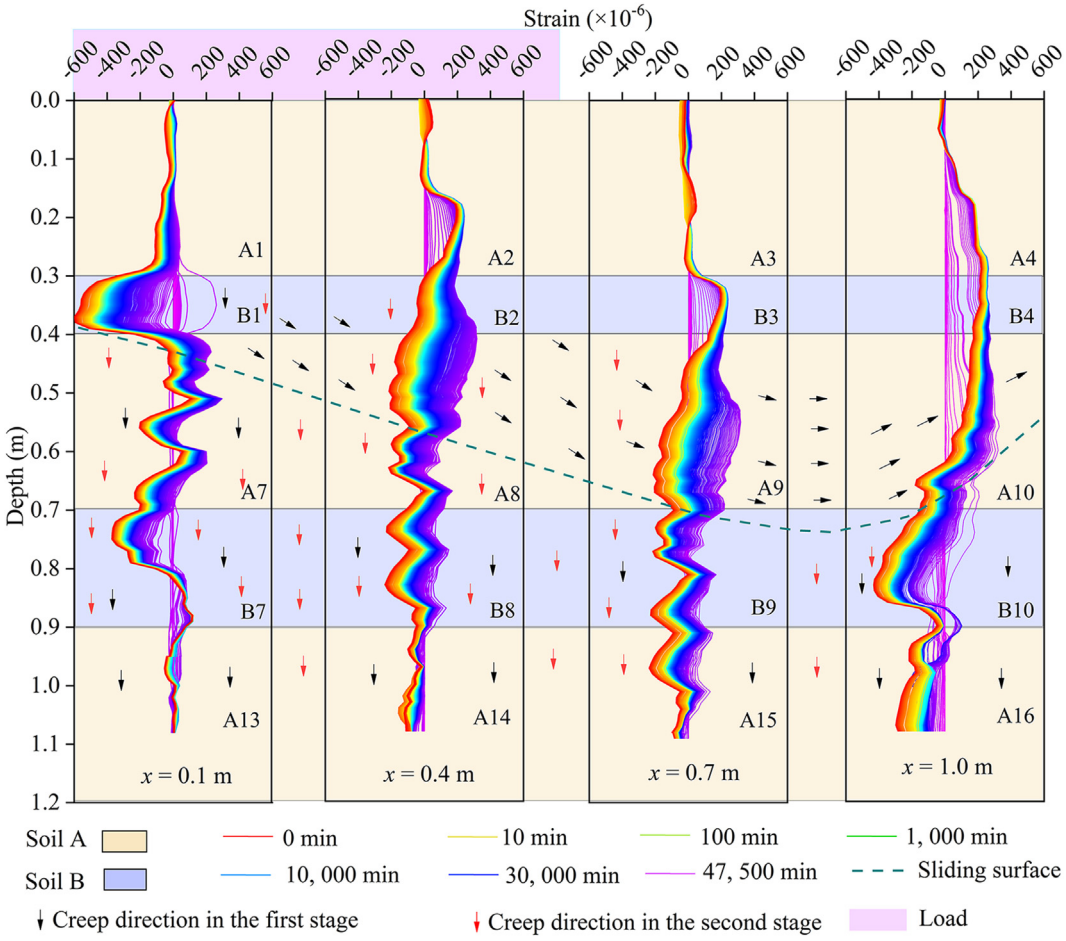

Fig. 12. Creep strain profiles measured using the OFDR.

3.3. Soil compression after groundwater table decline in the chamber

Because the compressive creep rate during the drainage process was rapid, it was necessary to collect data with a high temporal resolution. The OFDR interrogator used in this test had four channels and permitted only four SSCs to be connected. Thus, the strain profiles at $x = 0.1$ m, 0.4 m, 0.7 m, and 1 m, which are closely related to the load, were selected for monitoring. Fig. 12 shows the soil profiles during the dewatering process, which can be divided into the upper and lower parts using a dividing line (dotted line). The strain of the upper part increased rapidly and then gradually decreased, while the lower part was compressed during the entire period. This observation was consistent with Terzaghi's model (Fig. 9a). The dividing line in Fig. 12 is the sliding surface in the Terzaghi theory model. Terzaghi et al. (1996) introduced theories to determine the direction of soil particle movement and calculate the stability of foundations. In Terzaghi's model, the internal friction angle was assumed to be constant throughout the creep process. However, the observations in Fig. 12 show that this assumption was not valid in the early creep stage for the structure of calcareous sand (Fig. 9b). The drainage process can be divided into two stages, as for the corresponding deformation process. During the first stage, when the water table declined, the water in the large pores with good connectivity was rapidly removed, and the buoyancy vanished synchronously. The water removed from the poorly connected pores was slow; thus, the soil particles were surrounded by a water film and had a small sliding resistance. According to the theories of Terzaghi et al. (1996), the soil particles above the slide surface moved in the direction indicated by the black arrows in Fig. 12. The SSC was also dragged horizontally by the surrounding soil particles; therefore, the measured strain of the SSC increased rapidly. During the second stage, with the drainage of poorly connected pores, soil particles began to contact each other, resulting in a significantly enhanced frictional force. When the frictional force among soil particles increased, the particle deformation conformed to the model proposed by Bowman and Soga (2003), which agreed with the particle movement direction of the numerical results obtained by Yuan et al. (2018).

The soil deformation under the sliding surface in Terzaghi's model was neglected. According to the Terzaghi model, there was no horizontal deformation under the action of vertical compressive stress; otherwise, the sliding surface should move downward (Terzaghi et al., 1996). Thus, the soil beneath the sliding surface was only subjected to vertical compression, which can be verified by the observations in Fig. 12. The displacement and average strain of each soil layer were obtained by substituting the measured strain from Fig. 12 into Eqs. (2) and (3) (Fig. 13).

For the soil at the depths of 0.7–0.9 m and 0.9–1.2 m under the sliding surface, horizontal deformation (tensile strain) was very small, and vertical deformation (compressive strain) was significant. A slow transition from tensile to compressive strain was observed at depths of 0–0.3 m without noticeable inflection points, resulting from the action of capillary water. When the groundwater table declined, the water content in the capillary zone gradually decreased, but the decrease rate was significantly lower than that of

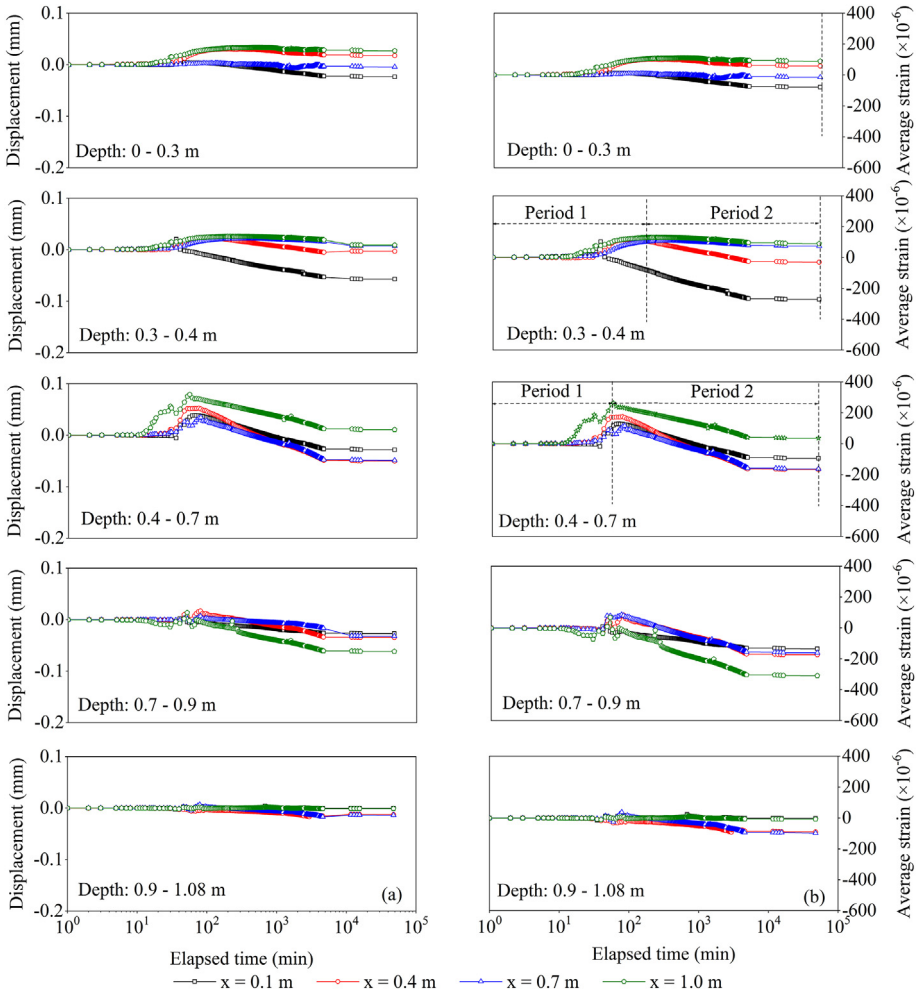

Fig. 13. Soil deformation of different layers: (a) Displacement, and (b) Average strain.

the groundwater table. There were apparent inflection points between the tensile and compressive strain periods. The tensile strain developed in Period 1, but in Period 2, the compressive strain increased. The shorter the Period 1, the earlier the drainage occurred. Period 1 of the soil at depths of 0.3–0.4 m and 0.4–0.7 m was 0–153 min and 0–152 min, respectively. The drainage time of the former was longer than that of the latter because the former contains kaolin, which reduces the hydrological conductivity. For the soil in the same layer, it would be easier to drain the zone that was closer to the drainage chamber, and its Period 1 was shorter. Period 1 was considered negligible when estimating compressive creep because it was significantly shorter than Period 2.

Two methods can be used to establish compressive creep models. The first is to connect the Kelvin body and Maxwell body in series or parallel, such as the Burgers and Yasong–Wang models in Table 3. In the Burgers model, the slope of the linear function term is significantly larger than that of the exponential function term; therefore, the Burgers model is also called a linear model (Yu et al., 2020). The causes of the total strain in the Yasong–Wang model account for grain rearrangement, particle sliding, and particle crushing, and each part is independently expressed. The second method is to establish an empirical formula, and the corresponding parameters are determined by laboratory calibration tests, such as the Fei–Wang and Yin models (Yin, 1999; Wang et al., 2012). Both the Fei–Wang and Yin models are logarithmic functions, and the difference is that there is a deformation limit in the latter but none in the former. After substituting the measured strain in Period 2 in Fig. 13 and the elapsed time into Eqs. (4)-(7), the evaluated strains of different creep models were obtained (Fig. 14). In Eqs. (4)-(7), only ε and t are variables, and all other parameters are constant and are fitted using the least-squares method. The R^2 values for each model are listed in Table 4.

Kuhn and Mitchell (1993) divided the soil creep process into the primary, secondary, and tertiary stages. The shear creep rate decreased, remained constant, and increased with time in the sequential primary, secondary, and tertiary stages, respectively. For compression deformation, creep exhibits a process of initial acceleration, then uniform speed, and finally deceleration to a stable process in a logarithmic time scale (Yin, 1999). The strain shown in Fig. 13 is the relative strain based on the start moment of the compression. During the primary creep stage, the predicted values of the Burger and Fei–Wang modes were biased from the measured values, but the bias for the Yasong–Wang and Yin models could be neglected. During the secondary stage, the predicted values of all four models agreed with the measured values. During the tertiary stage, the Burger and Yasong–Wang models had smaller errors than the Yin and Fei–Wang models. The R^2 in Table 4 indicates that the Yasong–Wang model had the best performance, followed by the Yin, Burger, and Fei–Wang models. The primary stage was only 50 min, which is of minimal significance in terms of the long-term performance of the engineering foundation, while the maximum settlement in the tertiary stage is an important reference for

Table 3
Typical compression creep models.

Model	Expression	Equation No.	Notation
Burger model (Yu et al., 2020)	$\varepsilon = \frac{q}{E_0} + \frac{q}{E_1}\left(1 - e^{-\frac{E_1}{\eta_1}t}\right) + \frac{q}{\eta_2}t$	(5)	ε: total strain; $\Delta\varepsilon$: strain increase due to creep only; $\Delta\varepsilon_L$: creep strain limit; ε_1: strain caused by grain rearrangement; ε_2: strain caused by particle sliding; ε_3: strain caused by particle crushing; η_1, η_2: viscosity coefficient; ψ_0': creep parameter; C, C_1 : integration constants; E_0: elastic modulus before creep; E_1: elastic modulus after creep; m: slope of linear in double logarithmic; q: vertical stress (kPa); q_H: horizontal stress (kPa); t: time variable (s); t_0: initial time (s)
Fei–Wang model (Wang et al., 2012)	$\varepsilon = \begin{cases} \frac{C}{1-m}t^{1-m} + C_1 & (m \neq 1) \\ C\ln t + C_1 & (m = 1) \end{cases}$	(6)	
Yasong–Wang model (Wang et al., 2019)	$\varepsilon = \varepsilon_1 + \varepsilon_2 + \varepsilon_3 = \frac{q}{E_1}\left(1 - e^{-\frac{E_1}{\eta_1}t}\right) + \frac{\sigma_1}{E_2}\left(1 - e^{-\frac{E_2}{\eta_1}t}\right) + \frac{q_H}{\eta_3}t$	(7)	
Yin model (Yin, 1999)	$\frac{\ln[(t+t_0)/t_0]}{\Delta\varepsilon} = \frac{1}{\psi_0'} + \frac{1}{\Delta\varepsilon_L}\ln\left(\frac{t+t_0}{t_0}\right)$	(8)	

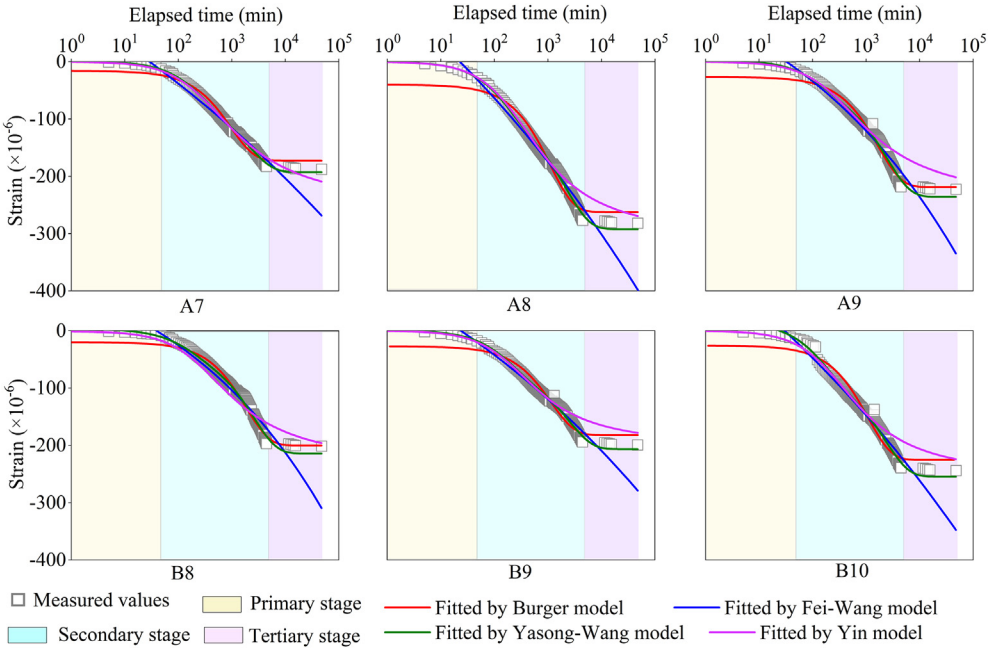

Fig. 14. Vertical strain versus log (time): comparison between measured values and estimated values fitted using the Burger, Fei–Wang, Yasong–Wang, and Yin models.

building design. When the load continues to increase, the interlock among particles will become smaller than the sliding force, and there will be no creep limit; thus, evaluations of the creep models will not be valid. All the R^2 values shown in Table 4 were larger than 0.9, indicating that the functional form of the existing model enabled the accurate description of the relationship between the creep strain and time, and most models were not used at the Kansai Airport because the model parameters are difficult to obtain accurately.

Table 4
R^2 of the soil compression creep models.

Model name	R^2 at different monitoring positions						
	A7	A8	A9	B8	B9	B10	Average R^2
Burger model	0.979	0.969	0.973	0.977	0.96	0.948	0.967
Fei–Wang model	0.957	0.96	0.94	0.935	0.96	0.946	0.95
Yasong–Wang model	0.998	0.997	0.993	0.991	0.994	0.986	0.993
Yin model	0.985	0.996	0.952	0.991	0.982	0.958	0.997

3.4. Deformation responses to groundwater change

To accurately describe the influence of the water level on soil deformation during the measurement period, the strain measured by OFDR on April 19, 2021, at 0:00, was used as the initial value, and the data measured over next 48 h were all different from the initial value. A positive strain indicates tension, and a negative one represents compression based on the initial value. Fig. 15 shows that the groundwater table periodically changed, with the highest at 20:00 and the lowest at around 8:00. Soil deformation primarily occurred in the range of groundwater table change (4.2–6.2 m), indicating that the groundwater table contributed significantly to soil deformation, which was consistent with the previous results in the literature that the compression–rebound deformation soil layer is close to the groundwater table change (Wu et al., 2021b).

The soil in this range was compressed when the groundwater table declined, and it subsequently swelled when the groundwater table rose, which was consistent with the laboratory results shown in Figs. 8 and 12. Additionally, tensile and compressive strains were

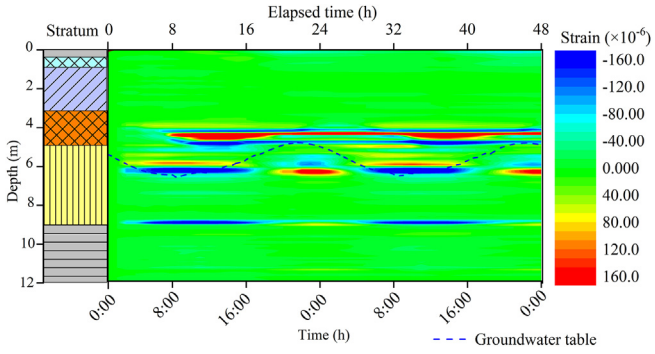

Fig. 15. Deformation of field layers to groundwater table fluctuation.

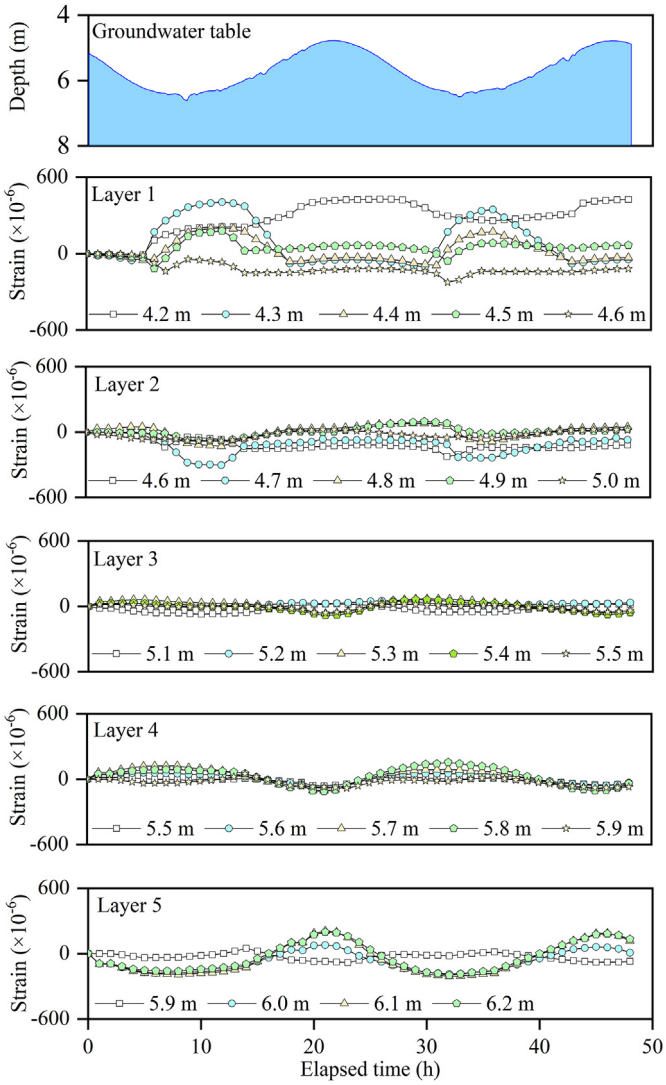

Fig. 16. Soil deformation with groundwater table at different locations.

observed to appear at intervals, indicating that the soil layer deformation at depth of 4.2–6.2 m was not coordinated. Fig. 16 shows the variation in the strain difference with time. The mixture of calcareous sand and clay at a depth of 4.2–6.2 m was divided into five layers numbered from 1 to 5, corresponding to depths of 4.2–4.6 m, 4.6–5 m, 5–5.5 m, 5.5–5.9 m, and 5.9–6.2 m. The strain of layer 3 hardly changed with time, suggesting that this layer had poor water absorption and large rigidity. The strain differences of layers 2 and 5 were positively correlated with the groundwater table, indicating that the deformation principle of these layers was the same as that of the soils used in the laboratory, which can be described by the compressive and swelling theory of Bowman and Soga (2003). The tensile strains of layers 1 and 4 were caused by the settlement of the adjacent layers. The closer to the lower compressed layer, the larger the tensile strain caused by collapse, which can be verified by the observations in layer 1 shown in Fig. 16.

According to the observations in Figs. 15 and 16, the natural coastal soil layers located between the highest and lowest groundwater tables are in cyclical compression and expansion, and the deformation of the upper vadose zone and lower saturation zone can be neglected. However, this repeated swelling–compression cycle can result in the loss of fine particles in artificial foundations, destroying the soil structure, and reducing the bearing capacity. Tuff interlayers are very common in the reclaimed foundations of the South China Sea, and they can significantly influence the deformation of adjacent calcareous sand layers. The tuff interlayers do not deform synergistically with the adjacent calcareous sand under the action of groundwater table variation, making it difficult for the current ground surface monitoring tools to observe. In addition, Fig. 15 shows that the soil located at the contact surface at a depth of 9 m deforms with the change of groundwater table. Thus, the range of groundwater table changes and the soil layer interface should be given special considerations when assessing the safety of calcareous sand foundations.

3.5. Uncertainty and potential applications

The uncertainty of calcareous sand foundation monitoring using OFDR relates to three aspects, i.e. installation of fiber optic sensors, large deformation test, and pre-tensioning. All the reported fiber optic sensors used in the ground subsidence monitoring were installed in boreholes. However, the boreholes in coral calcareous sand foundations are prone to being collapsed, making it difficult to lay sensors. The field measured data of the settlement occurred on the islands located in the South China Sea has not yet been reported. Taking the Kansai Airport as the case, the total settlement of 23 m will significantly exceed the maximum measurement range of OFDR (2%). When using an optical fiber to monitor soil deformation, the optical fiber must be stretched to an elastic strain and then fixed. Soil compression is determined by the amount of rebounding. However, if the depth of a borehole is too large, the weight of optical fiber itself cannot be ignored, resulting in a large difference in stretching strain.

The significance of OFDR monitoring results is to locate the deformation position and capture strain profiles. As the traditional technology can only acquire the ground surface settlement, there are different opinions on whether the sand layer rebounds after groundwater table rising. Thus, the continuous strain obtained by OFDR is helpful in ending this controversy. The results in Fig. 12 show that the OFDR monitoring data can accurately locate the sliding surface and the plastic zones beneath a footing, and they can be used to optimize the width and depth of the footing. The observations in Fig. 15 indicate that the soil in the range of groundwater table fluctuation periodically deforms, which may cause the loss of fine particles. Therefore, this zone should be given more attention during the foundation treatment process. Common treatments include replacement, grouting, or the use of piles.

4. Conclusions

In this study, a laboratory model test and an in situ monitoring test were conducted. The feasibility of using an OFDR to capture strain profiles in coral calcareous sand foundations was verified. The deformation response to groundwater table and load variation was investigated. The optimum creep model for describing the swelling and compression of a calcareous sand foundation was selected, and the characteristics of in situ foundation deformation were discussed. Based on the results and discussions presented earlier, the following general conclusions can be drawn:

(1) The OFDR can capture strain profiles with a high spatial resolution (±1 mm) and accurately locate the swelling and compressive zones in the calcareous sand foundation under different conditions of loading and groundwater table fluctuation both in the laboratory model chamber and in situ soil layers.
(2) The interlock between calcareous sand particles can be acquired using an OFDR, which affects the particle movement direction, resulting in the shape change of the elastic and plastic zones in the foundation. Under the influence of interlock, the foundation can be divided into two parts based on the sliding surface. Above the sliding surface, soil particles moved up diagonally. When the particles move and roll, an interlocking effect occurs, resulting in a significant increase in the friction between the particles. Thus, the deformation above the sliding surface is dominated by compression. Beneath the sliding surface, the soil is continuously compressed.
(3) The strain profiles measured using the OFDR indicate that the calcareous sand swelling processes above and beneath the groundwater table are significantly different, due to different expansion mechanisms. The swelling of soil beneath the groundwater table is completed rapidly, which is determined by the equilibrium of gravity, particle surface friction, and buoyancy. Soil swelling above the water table occurs gradually and is primarily determined by capillary water.
(4) When the groundwater level and load remain constant, the compression creep rate of calcareous sand first gradually increases, then remains constant, and finally tends to be zero on a logarithmic time scale, which can be described by the Yasong-Wang model with $R^2 = 0.993$.
(5) The in situ soil deformation primarily occurs between the highest and lowest groundwater tables, which periodically varies with the groundwater table fluctuation. The calcareous sand is compressed when the groundwater table declines and swells when the groundwater table ascends. The tuff interlayers with poor water absorption capacity do not swell or compress, but they can produce a settlement or lift under the influence of adjacent deformed calcareous sand layers.

Declaration of competing interest

The authors declare that they have no known competing financial interests or personal relationships that could have appeared to influence the work reported in this paper.

Acknowledgments

Financial support provided by the National Natural Science Foundation of China (Grant No. 41907244), China Postdoctoral Science Foundation (Grant No. 2019M653180), and the Project of the Key Laboratory of Soft Soil and Environmental Geotechnical Ministry of Education (Grant No. 2019P05) is gratefully acknowledged.

References

Ahmadi, S., Kamalian, M., Askari, F., 2021. Evaluation of the static bearing capacity coefficients of rough strip footing using the stress characteristics method. Int. J. Civ. Eng. 19 (2), 155–165.
Al-Hashemi, H.M., Al-Amoudi, O.S.B., 2018. A review on the angle of repose of granular materials. Powder Technol. 330, 397–417.
Boujia, N., Schmidt, F., Chevalier, C., Siegert, D., Bang, D.P.V., 2020. Distributed optical fiber-based approach for soil-structure interaction. Sensors 20 (1), 321.
Bowman, E., Soga, K., 2003. Creep, ageing and microstructural change in dense granular materials. Soils Found. 43 (4), 107–117.
Cao, D.F., Zhu, H.H., Wu, B., Wang, J.C., Shukla, S.K., 2021. Investigating temperature and moisture profiles of seasonally frozen soil under different land covers using actively heated fiber Bragg grating sensors. Eng. Geol. 290, 106197.
Catalao, J., Raju, D., Nico, G., 2020. InSAR maps of land subsidence and sea level scenarios to quantify the flood inundation risk in coastal cities: the case of Singapore. Rem. Sens. 12 (2), 296.
Feng, W.Q., Lalit, B., Yin, Z.Y., Yin, J.H., 2017. Long-term non-linear creep and swelling behavior of Hong Kong marine deposits in oedometer condition. Comput. Geotech. 84, 1–15.
Gu, K., Shi, B., Liu, C., Jiang, H.T., Li, T.B., Wu, J.H., 2018. Investigation of land subsidence with the combination of distributed fiber optic sensing techniques and microstructure analysis of soils. Eng. Geol. 240, 34–47.
Gu, Y.Y., Zhou, D.W., Zhang, D.M., Wu, K., Zhou, B.H., 2020. Study on subsidence monitoring technology using terrestrial 3D laser scanning without a target in a mining area: an example of Wangjiata coal mine, China. Bull. Eng. Geol. Environ. 79, 3575–3583.
He, S.H., Ding, Z., Xia, T.D., Zhou, W.H., Gan, X.L., Chen, Y.Z., Xia, F., 2020. Long-term behaviour and degradation of calcareous sand under cyclic loading. Eng. Geol. 276, 105756.
Henault, J.M., Quiertant, M., Delepine-Lesoille, S., Salin, J., Moreau, G., Taillade, F., Benzarti, K., 2012. Quantitative strain measurement and crack detection in RC structures using a truly distributed fiber optic sensing system. Construct. Build. Mater. 37, 916–923.
Kuang, D., Long, Z.L., Guo, R.Q., Yu, P.Y., 2020. Experimental and numerical investigation on size effect on crushing behaviors of single calcareous sand particles. Mar. Georesour. Geotechnol. 39 (5), 543–553.
Kuhn, M.R., Mitchell, J.K., 1993. New perspectives on soil creep. J. Geotech. Eng. 119 (3), 507–524.
Kwon, Y.S., Seo, D.C., Choi, B.H., Jeon, M.Y., Kwon, I.B., 2018. Strain measurement distributed on a ground anchor bearing plate by fiber optic OFDR sensor. Appl. Sci. 8 (11), 2051.
Liu, J., Song, Z.Z., Lu, Y., Bai, Y.X., Qian, W., Kanungo, D.P., Chen, Z.H., Wang, Y., 2019. Monitoring of vertical deformation response to water draining–recharging conditions using BOFDA-based distributed optical fiber sensors. Environ. Earth Sci. 78, 406.
Liu, L.M., Yu, J., Chen, B.B., Wang, Y.B., 2020. Urban subsidence monitoring by SBAS-InSAR technique with multi-platform SAR images: a case study of Beijing Plain, China. Eur. J. Remote Sens. 53, 141–153.
Lv, Y.R., Li, F., Liu, Y.W., Fan, P.X., Wang, M.T., 2017. Comparative study of coral sand and silica sand in creep under general stress states. Can. Geotech. J. 54 (11), 1601–1611.
Mesri, G., Funk, J.R., 2015. Settlement of the Kansai international airport islands. J. Geotech. Geoenviron. Eng. 141 (2), 04014102.
Pelecanos, L., Soga, K., Elshafie, M.Z.E.B., Battista, N., Kechavarzi, C., Gue, C.Y., Ouyang, Y., Seo, H.J., 2018. Distributed fiber optic sensing of axially loaded bored piles. J. Geotech. Geoenviron. Eng. 144 (3), 04017122.
Shahnazari, H., Rezvani, R., 2013. Effective parameters for the particle breakage of calcareous sands: an experimental study. Eng. Geol. 159, 98–105.
Song, Z.P., Shi, B., Juang, H., Shen, M.F., Zhu, H.H., 2017. Soil strain-field and stability analysis of cut slope based on optical fiber measurement. Bull. Eng. Geol. Environ. 76 (3), 937–946.
Terzaghi, K., Peck, R.B., Mesri, G., 1996. Soil Mechanics in Engineering Practice. John Wiley & Sons, Inc., New York, USA.
Wang, F., Miao, L.C., Zhang, Y.J., 2012. A simplified method to predict creep behavior of the Yangtze River sand. Bull. Eng. Geol. Environ. 71 (2), 317–324.
Wang, X.Z., Weng, Y.L., Wei, H.Z., Meng, Q.S., Hu, M.J., 2019. Particle obstruction and crushing of dredged calcareous soil in the Nansha Islands, South China Sea. Eng. Geol. 261, 105274.
Wang, P., Liu, Y.M., 2021. Research and application of an improved internal thrust force measurement system for rock and soil mass based on OFDR. Geomatics, Nat. Hazards Risk 12 (1), 1426–1448.
Wang, D.Y., Zhu, H.H., Wang, B.J., Shi, B., 2021. Performance evaluation of buried pipe under loading using fiber Bragg grating and particle image velocimetry techniques. Measurement 186, 110086.
Wu, J.H., Shi, B., Cao, D.F., Jiang, H.T., Wang, X.F., Gu, K., 2017. Model test of soil deformation response to draining-recharging conditions based on. DFOS. Eng. Geol. 226, 107–121.
Wu, H., Zhu, H.H., Zhang, C.C., Zhou, G.Y., Zhu, B., Zhang, W., Azarafza, M., 2020. Strain integration-based soil shear displacement measurement using high-resolution strain sensing technology. Measurement 166, 108210.

Wu, Y., Li, N., Wang, X.Z., Cui, J., Chen, Y.L., Wu, Y.H., Yamamoto, H., 2021a. Experimental investigation on mechanical behavior and particle crushing of calcareous sand retrieved from South China Sea. Eng. Geol. 280, 105932.
Wu, J.H., Shi, B., Gu, K., Liu, S.P., Wei, G.Q., 2021b. Evaluation of land subsidence potential by linking subsurface deformation to microstructure characteristics in Suzhou, China. Bull. Eng. Geol. Environ. 80 (3), 2587–2600.
Yin, J.H., 1999. Non-linear creep of soils in oedometer tests. Geotech 49 (5), 699–707.
Yu, D.W., Ye, J.H., Yao, L.H., 2020. Prediction of the long-term settlement of the structures built on a reclaimed coral reef island: an aircraft runway. Bull. Eng. Geol. Environ. 79 (9), 4549–4564.
Yuan, R., Yu, H.S., Hu, N., He, Y., 2018. Non-coaxial soil model with an anisotropic yield criterion and its application to the analysis of strip footing problems. Comput. Geotech. 99, 80–92.
Zamanian, M., Jafarzadeh, F., 2020. Experimental study of stress anisotropy and noncoaxiality of dense sand subjected to monotonic and cyclic loading. Transp. Geotech. 23, 100331.
Zhang, C.C., Zhu, H.H., Liu, S.P., Shi, B., Zhang, D., 2018a. A kinematic method for calculating shear displacements of landslides using distributed fiber optic strain measurements. Eng. Geol. 234, 83–96.
Zhang, C.C., Shi, B., Gu, K., Liu, S.P., Wu, J.H., Zhang, S., Zhang, L., Jiang, H.T., Wei, G.Q., 2018b. Vertically distributed sensing of deformation using fiber optic sensing. Geophys. Res. Lett. 45 (21), 711–732.
Zhang, L., Shi, B., Zhu, H.H., Yu, X.B., Han, H.M., Fan, X.D., 2021. PSO-SVM-based deep displacement prediction of Majiagou landslide considering the deformation hysteresis effect. Landslides 18, 179–193.
Zhu, H.H., Shi, B., Zhang, J., Yan, J.F., Zhang, C.C., 2014. Distributed fiber optic monitoring and stability analysis of a model slope under surcharge loading. J. Mt. Sci. 11, 979–989.
Zhu, H.H., Wang, Z.Y., Shi, B., Wong, J.K.W., 2016. Feasibility study of strain based stability evaluation of locally loaded slopes: insights from physical and numerical modeling. Eng. Geol. 208, 39–50.

Dingfeng Cao received his BSc degree in Engineering Geology from Lanzhou University, China, in 2011, and his MSc and PhD degrees from the School of Earth Science and Engineering in Nanjing University, China, in 2014 and 2018, respectively. He is a Postdoctoral fellow of Sun Yat-sen University from 2018 to 2021. His research interests include: (1) soil moisture content monitoring using actively heated fiber optic method, (2) calcareous foundation settlement evaluation, and (3) multi-field coupling.